Physics Understanding and Solutions to Key Issues of Long-Pulse High-Performance Operation on EAST

J. Huang[1], X. Gong[1], B. Zhang[1], R. Ding[1], X.J. Zhang[1], L. Zeng[2], Z.H. Wang[2], M.H. Li[1], L.Q. Xu[1], Y.F. Wang[1], X. Jian[1], C.Y. Pan[1], W. Wang[1], L.Y. Chen[1], Y.C. Hu[1], H.D. Xu[1], W.B. Liu[1], Y.W. Yu[1], K.D. Li[1], P. Li[1], M. Jia[1], T.Q. Jia[1], G.Z. Zuo[1], F. Ding[1], S.X. Wang[1], H.L. Zhao[1], Y.M. Duan[1], Y.F. Jin[1], H.M. Zhang[1], Z.C. Lin[1], G.L. Xu[1], Q.P.Yuan[1], Y. Huang[1], Y. Sun[1], Q.L. Ren[1], Q. Zang[1], L. Zhang[1], G.Q. Li[1], D.M. Yao[1], L. Wang[1], H.Q. Liu[1], Q.Q. Yang[1], J.P. Qian[1],G.S. Xu[1], J.S. Hu[1], K. Lu[1], Y.T. Song[1], B.N. Wan[1], J.G. Li[1] and the EAST Team

[1] *Institute of Plasma Physics, CAS, Hefei, China*

[2] *Tsinghua University, Beijing, China*

Abstract

EAST has realized steady-state high-performance H-mode plasma sustained for a record 1066 s with a total injected energy of 3.05 GJ, setting a new world record for kilosecond-scale long-pulse tokamak operation. This milestone is enabled by the integration of fully water-cooled tungsten plasma-facing components (W-PFCs), high-efficiency radio-frequency (RF) heating and current drive (H&CD), high-precision plasma equilibrium feedback control, real-time in-situ wall conditioning, and integrated core-edge plasma physics. The record discharge was achieved in a lower single-null (LSN) configuration with a poloidal beta $\beta_P = 2.0$ and bootstrap current fraction $f_{\mathrm{BS}} \approx 50\%$, driven by a lower hybrid current drive (LHCD) power of 1.1 MW and an electron cyclotron resonance heating (ECRH) power of 1.9 MW. The synergistic coupling between on-axis ECRH and LHCD plays a critical role in sustaining high-confinement plasma states. A stable small edge-localized mode (small-ELM) operational window was accessed by placing the outer strike point on the horizontal tungsten divertor target, which improves RF power coupling efficiency and mitigates tungsten sputtering and surface erosion. Fully non-inductive plasma current sustainment was maintained at an electron density reaching 63% of the Greenwald limit ($n_e/n_G = 0.63$). A spontaneously formed electron temperature internal transport barrier (e-ITB) yields a confinement enhancement factor $H_{98,y2} = 1.3$. The e-ITB-based H-mode discharge exhibits nonlinear self-organization behaviors near the magnetic axis without external momentum injection, and a saturated $m/n = 1/1$ kink (SSK) mode sustains high-T_e plasma with improved confinement. This work elaborates the underlying physical mechanisms and enabling engineering upgrades of EAST, delivering critical experimental benchmarks for steady-state operation scenarios applicable to ITER and CFEDR.

Keywords: EAST; long-pulse steady-state; H-mode; e-ITB; tungsten divertor; bootstrap current; RF synergy; core-edge integration

1. Introduction

The integration of high plasma confinement performance and ultra-long pulse duration stands as one of the core challenges for magnetic confinement fusion energy research. Sustained long-pulse operation demands coordinated control over multiple coupled subsystems: kinetic and magnetic equilibrium, continuous RF heating and current drive, active fuel injection and exhaust pumping, heat dissipation via actively cooled plasma-facing components (PFCs), and long-timescale plasma–wall interactions (PWIs) far exceeding the energy confinement time [1]. For ITER and future commercial fusion reactors, steady-state or long-pulse operational scenarios must simultaneously achieve high plasma confinement, a large non-inductive current fraction, compatible divertor exhaust capability, and reliable real-time plasma control [2].

EAST has achieved a landmark steady-state high-performance H-mode plasma discharge lasting 1066 s under reactor-relevant operational conditions. The discharge achieves an $H_{98,y2}$ factor of approximately 1.35, a normalized density $n_e/n_G \approx 0.6$, a bootstrap current fraction $f_{\mathrm{BS}} \approx 50\%$, and a central electron temperature $T_e(0) \approx 10\mathrm{keV}$, with a total injected heating energy of 3.05 GJ, while maintaining fully non-inductive current operation and well-controlled boundary plasma conditions. This breakthrough extends EAST's long-pulse performance benchmarks built on prior 100 s and 310 s high-performance H-mode discharges, moving steadily toward reactor-relevant kilosecond operating conditions [3–5]. Multiple advanced supporting systems have been fully integrated in this experiment: the full-tungsten limiter and divertor equipped with active water-cooling systems significantly enhances heat flux bearing and removal capabilities [6]; robust real-time plasma control systems stabilize plasma shape, X-point, and strike-point positions over ultra-long timescales [7]; optimized fueling, pumping, and real-time lithium powder injection regulate particle recycling and impurity sources beyond the wall saturation timescale [8,9].

On this basis, three interrelated fundamental physics challenges remain to be resolved for steady-state H-mode operation. First, heating and current-drive efficiency need to be enhanced by optimizing lower hybrid wave (LHW) accessibility and EC–LH synergistic effects under high-density conditions [10]. Second, it is essential to uncover the self-organization mechanism of high-T_e core plasmas with negligible external torque injection, which is governed by couplings among microturbulence, magnetic shear, fast electrons, and saturated kink modes. Third, robust core-edge integration must be maintained to simultaneously sustain high core confinement, favorable small-ELM pedestal dynamics, and effective tungsten impurity control throughout kilosecond-scale H-mode discharges.

2. Demonstration of Long Pulse Fully Non-Inductive H-mode Plasma Operation

2.1 Overview of the World-Record 1066 s H-mode Experiment

Recently, EAST attained a landmark experimental milestone: a world-record H-mode plasma discharge sustained for 1066 s with a total injected heating energy of approximately 3.05 GJ. This achievement makes EAST the world's first tokamak that can simultaneously realize three core steady-state fusion characteristics: kilosecond-scale pulse duration, ten-million-degree plasma temperature, and high-fraction fully non-inductive current sustainment. This long-duration stable H-mode operation is enabled by comprehensive advances in plasma physics and engineering technologies, including low-momentum RF heating and current drive, tungsten impurity suppression under full-metal wall reactor conditions, active divertor heat flux and particle exhaust regulation, precise plasma–wall interaction control, global particle balance management, and long-term sustainment of magnetic configuration and equilibrium stability.

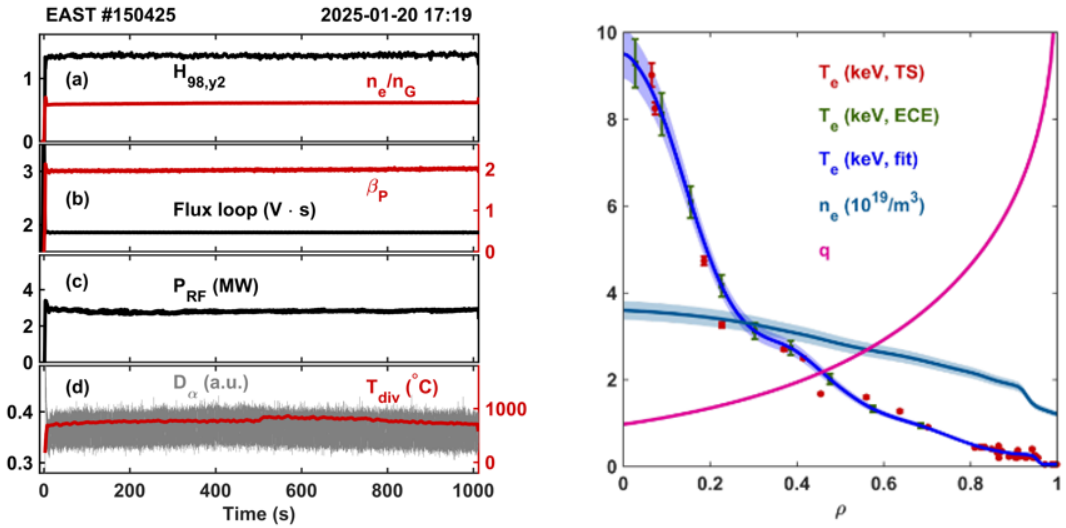

Figure 1 Time evolution of key plasma parameters for the 1066 s long-pulse H-mode discharge on EAST (Left), (a) $H_{98,y2}$ and normalized electron density n_e/n_G, (b) Poloidal flux and β_P, (c) the total injected RF power, (d) Divertor temperature (IR) and D_α emission. Electron density and temperature and current density profiles (Right).

Systematic technical solutions have been implemented to address the critical challenges of 1066 s long-pulse H-mode operation, as illustrated in Figure 1. This experiment adopts an LSN magnetic configuration, with the outer strike point positioned on the horizontal tungsten divertor target. Key machine and plasma parameters for this discharge are summarized below: plasma current $I_p = 0.3$MA, edge safety factor $q_{95} \approx 8.3$, toroidal magnetic field $B_t = 2.5$T, major radius $R = 1.85$m, and minor

radius$a = 0.45$m. The total RF heating power reaches 3.0 MW, consisting of 1.1 MW LHCD power and 1.9 MW ECRH power, yielding a poloidal beta $\beta_P = 2.0$. Fully non-inductive current sustainment is achieved at an electron density corresponding to 60% of the Greenwald density limit. A spontaneously generated e-ITB forms in the plasma core, raising the confinement enhancement factor $H_{98,y2}$ above 1.3.

By suppressing wall particle recycling to flatten the edge density profile, we accessed a stable small-ELM operating window, identifiable by the nearly flat D_α emission trace in Figure 1(d). This operational regime provides two complementary advantages: it improves LHW power coupling efficiency and suppresses tungsten sputtering and erosion to reduce edge tungsten impurity sources. Core electron temperature diagnosed via electron cyclotron emission (ECE) and Thomson scattering (TS) reaches approximately 10 keV, satisfying reactor-relevant thermal conditions. The flattened core density profile makes trapped electron mode (TEM) turbulence the dominant core thermal transport mechanism, which drives outward radial transport of high-Z tungsten impurities, thereby preventing core tungsten impurity accumulation.

2.2 Integrated Engineering Solutions for Thousand-Second Long-Pulse Operation

The 1066-sencond high-performance H-mode discharge is realized via a core-edge integrated steady-state control strategy: small ELMs suppress edge tungsten impurity sources, while optimized plasma profiles regulate core tungsten transport, fundamentally resolving the tungsten impurity confinement challenge in fusion plasmas. Combined with low-Z wall coating and real-time lithium powder feedback injection for enhanced particle control, no core tungsten accumulation is observed throughout the entire discharge pulse.

Based on EAST's full set of actively cooled tungsten PFCs, four integrated engineering strategies are developed to tackle four critical steady-state operational issues: heat exhaust, magnetic drift, wall recycling saturation, and tungsten accumulation. The lower divertor adopts a composite structure composed of 3/4 monoblock tungsten targets and 1/4 flat tungsten targets, and all ion cyclotron resonance frequency (ICRF) and LHW antenna limiters are manufactured from tungsten. The active cooling system can withstand a steady-state heat flux of 10–20 MW/m². The carbon-free all-tungsten first wall enables low-contamination long-pulse operation consistent with practical fusion reactor conditions.

A multi-layer closed-loop feedback control system was deployed to mitigate typical long-pulse operational anomalies, such as magnetic integrator drift, poloidal field (PF) coil current drift, vertical plasma instability, and plasma shape deformation. The conventional ~400 s pulse duration limit induced

by particle balance and wall saturation is overcome through multi-channel collaborative regulation, including supersonic molecular beam injection (SMBI), dome gas puffing, and real-time lithium powder feedback injection, enabling stable particle recycling control beyond the wall saturation timescale, shown in figure 3.

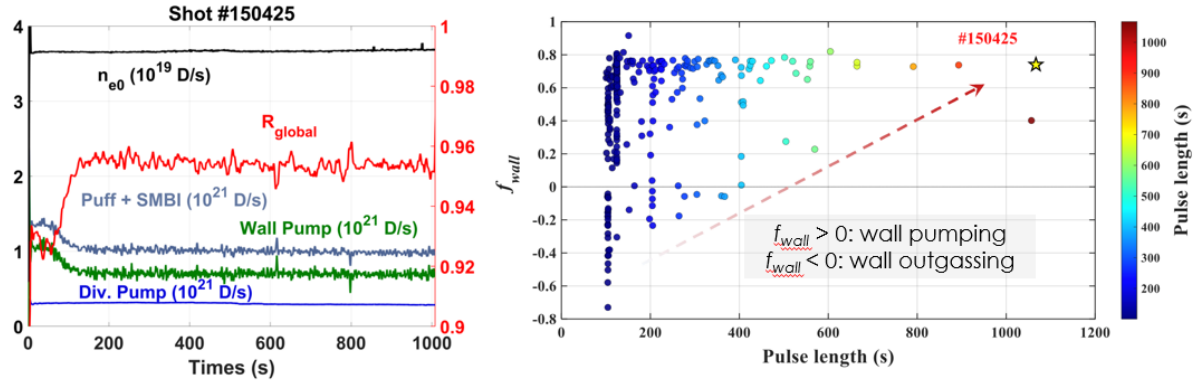

Figure 2 (left)Time evolution of various particle source and pumping during the long pulse discharge, including center plasma density (n_{e0}), external gas injection rate including gas puffing and Supersonic Molecular Beam Injection (Puff + SMBI), divertor pumping rate via cryopumps (Div. Pump), and wall pumping rate (wall pump), and global recycling coefficient R_{global} (left). Wall pumping capability played a significant role over 1000s, t_{dur} < 400s can survive with wall outgassing, t_{dur} >400-100s, needs sufficient wall pumping (right)

EAST's long-pulse high-performance steady-state experimental results provide critical experimental data and engineering support for future commercial fusion reactors. The integrated technical route combining advanced plasma feedback control, high-power RF H&CD systems, and optimized magnetic configurations meets ITER's steady-state long-pulse operational requirements and supports the achievement of fusion gain $Q \geq 5$.

3. PHYSICS ISSUES AND UNDERSTANDING OF LONG-PULSE H-MODE PLASMA

3.1 Improved H&CD efficiency at high density

For the 1066 s long-pulse H-mode plasma, fully non-inductive plasma operation is sustained by pure RF heating power ($P_{\mathrm{RF}} \approx 3.0$MW, including $P_{\mathrm{LHCD}} \approx 1.1$MW and $P_{\mathrm{ECRH}} \approx 1.9$MW) at a normalized density $n_e/n_{\mathrm{GW}} \approx 0.63$. The LHW power spectrum directly determines wave accessibility and deposition characteristics. Waves with a parallel refractive index $N_{\parallel}$ below the accessibility threshold $N_{\parallel,\mathrm{acc}}$ are converted into fast waves and reflected toward the plasma edge. Therefore, the launched LHW spectrum must strictly satisfy the accessibility criterion [11]:

$$N_{||acc} = \frac{\omega_{pe}}{\omega_{ce}} + \sqrt{1 + (\frac{\omega_{pe}}{\omega_{ce}})^2 - (\frac{\omega_{pi}}{\omega})^2} \qquad (1)$$

Meanwhile, the launched parallel refractive index $N_{\|}$ should not be excessively large, as the current-drive efficiency scales roughly with$1/N_{\|}^2$ following Fisch's classic current-drive theory [12]. Here, ω_{pe} and ω_{pi} denote the local electron and ion plasma frequencies, ω_{ce} represents the local electron cyclotron frequency, and ω is the LHW angular frequency. For the long-pulse H-mode discharge with a central electron density $n_{e0} \approx 3.6 \times 10^{19}\mathrm{m}^{-3}$, the optimal $N_{\|}$ is approximately 2.04, which is slightly higher than $N_{\|,\mathrm{acc}}$ and corresponds to the 90° antenna phasing shown in Figure 3. This optimized spectrum ensures excellent core wave accessibility while maintaining a high co-current directivity of 76.8%.

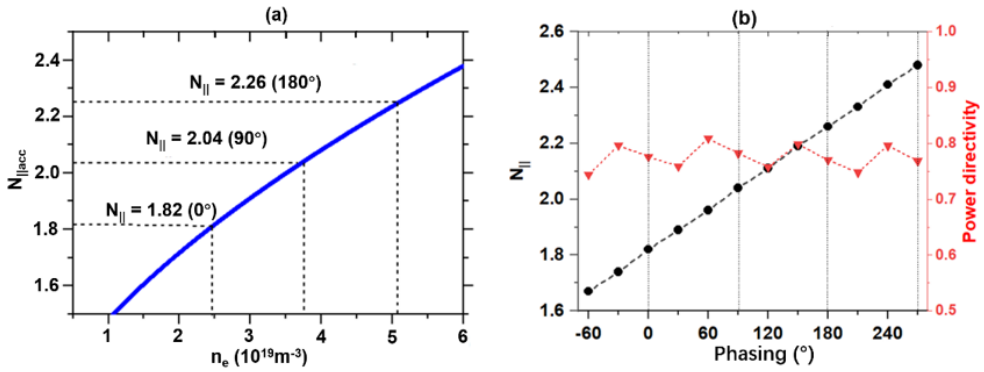

Figure 3. Accessibility criterion $N_{||acc}$ of LH wave at 4.6 GHz as a function of electron density with B_t = 2.5 T (a); $N_{||}$ peak and power directivity versus LH antenna phasing.

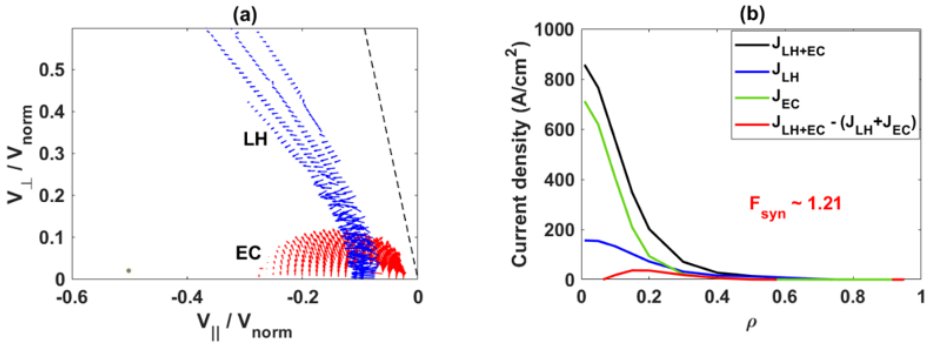

Figure 4. Particle flux vector due to LH (blue) and EC (red) waves in 2D momentum space (a); current density profiles calculated by GENRAY/CQL3D for discharges #150425 (b).

The ECRH deposition location also plays a dominant role in heating efficiency. On-axis ECRH deposition at $B_t \approx 2.5$T is favorable for achieving elevated plasma confinement at 140 GHz [13]. GENRAY/CQL3D simulations verify moderate synergistic effects between LHCD and ECCD induced

by velocity-space diffusion, as presented in Figure 4. The LH–EC synergy factor is defined as $F_{syn} = (I_{LH+EC} - I_{LH} - I_{EC})/I_{EC}$, which reaches 1.21 in this discharge. Here, I_{LH+EC} denotes the total non-inductive current driven by simultaneous LHW and ECRH injection, while I_{LH} and I_{EC} correspond to currents driven by individual wave systems.

The EC heating effect is also strongly controlled by the deposition location, and on-axis deposition at B_t ~ 2.5 T is favorable for higher confinement at 140 GHz [13]. GENRAY/CQL3D simulations show a moderate LHCD-ECCD synergy caused by velocity-space diffusion, as shown in Fig. 4. The synergy factor $F_{syn} = I/I_{EC} = (I_{LH+EC} - I_{LH} - I_{EC})/I_{EC}$ is about 1.21, where I_{LH+EC} is the current driven by combined LH and EC waves and I_{LH} and I_{EC} are the separately driven LH and EC currents.

3.2 Improved Confinement with Zero Torque Injection

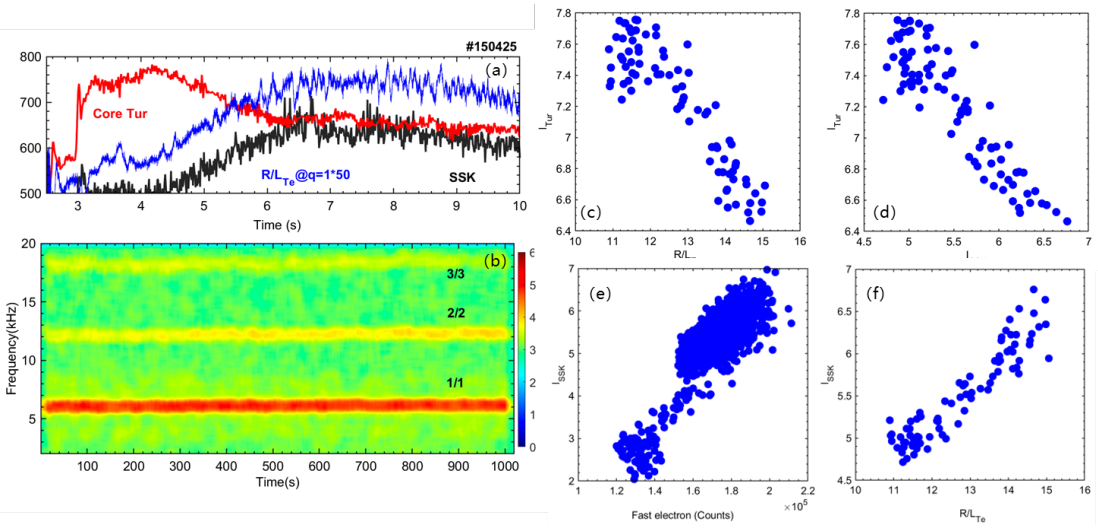

Figure 5. Self-organization of the SSK and core turbulence in #150425. (a,b) Evolution of core turbulence, electron-temperature-gradient-related quantities and SSK signals, together with the corresponding spectrum; (c,d) statistical competition between the SSK and core turbulence; (e,f) relation of the SSK intensity to the fast-electron signal and electron-temperature-gradient-related drive.

In the #150425 discharge dominated by ECRH heating, the normalized electron-temperature gradient enters a high-gradient regime, exciting core electron temperature gradient (ETG) turbulence prior to the growth of the saturated $m/n = 1/1$ kink (SSK) mode near the $q = 1$ magnetic surface. As illustrated in Figure 5(a,b), the SSK evolves into a long-lived nonlinear saturated state, after which microturbulence amplitude decreases while the high core temperature gradient is well preserved. This indicates that the SSK acts as an active regulator of turbulence, magnetic shear, and current profiles, rather than a passive

residual perturbation, which is consistent with previous EAST studies on SSK saturation and nonlinear magnetohydrodynamic (MHD) evolution [14,15].

Correlations displayed in Figure 5(c,d) demonstrate that core microturbulence intensity declines with rising electron-temperature gradient and SSK amplitude. Since the temperature gradient remains high after SSK saturation, the turbulence suppression is not attributed to weakened gradient drive. Instead, a portion of the gradient free energy is transferred from small-scale microturbulence to low-frequency MHD modes. Figure 5(e,f) further confirms the positive correlation between SSK intensity, fast-electron signals, and electron-temperature-gradient drive, verifying that fast-electron redistribution contributes to SSK sustainment [16].

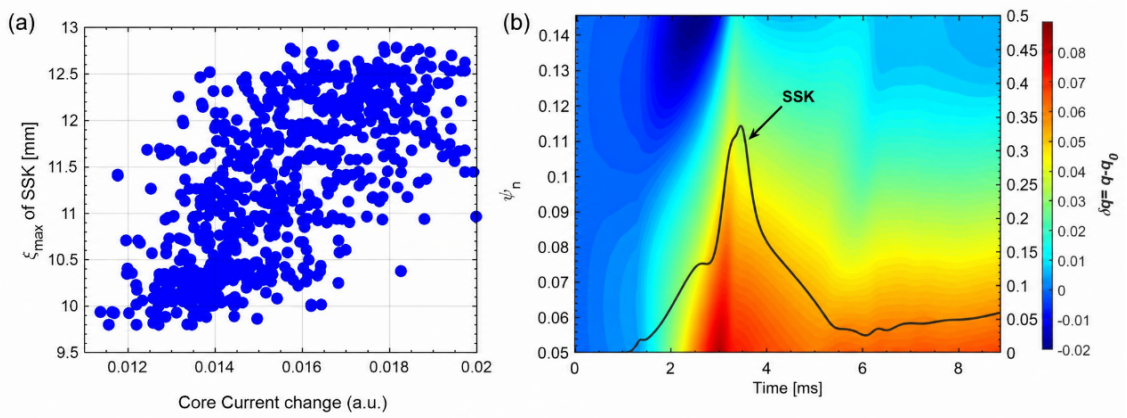

Figure 6. Experimental and simulation evidence for the SSK magnetic flux-pumping effect. (a) Experimental relation between the maximum SSK displacement and the core current change; (b) M3D-C1 simulation result showing q-profile modulation induced by the SSK.

Magnetic flux pumping serves as the critical intermediate link in this plasma self-organization process. As shown in Figure 6, larger SSK displacement corresponds to more significant modulation of the core current profile. Nonlinear MHD simulations further reveal that the SSK modulates the local $\boldsymbol{q}$ profile and reduces central magnetic shear. Therefore, the SSK indirectly suppresses turbulent transport by redistributing plasma current and maintaining weak central magnetic shear, which disfavors small-scale turbulent development, consistent with intrinsic current observations and flux-pumping simulation results [17,18].

The self-organized physical feedback chain can be summarized concisely: high core electron temperature and off-axis pressure gradients excite microturbulence and trigger SSK growth; after SSK nonlinear saturation, energy competition and weakened magnetic shear suppress turbulent transport; magnetic flux pumping further sustains low central magnetic shear, and the resultant improved confinement preserves the high-T_e core plasma.

3.3 Core-Edge Integration

Pedestal stability of the #150425 discharge was analyzed using the ELITE code during the inter-ELM phase at approximately 500 s [19]. A kinetic equilibrium was reconstructed by mapping EAST experimental profile data onto normalized poloidal flux based on EFIT equilibrium reconstruction results [20]. The pedestal profiles were fitted with a modified hyperbolic tangent function, while core profiles were fitted via spline interpolation [21].

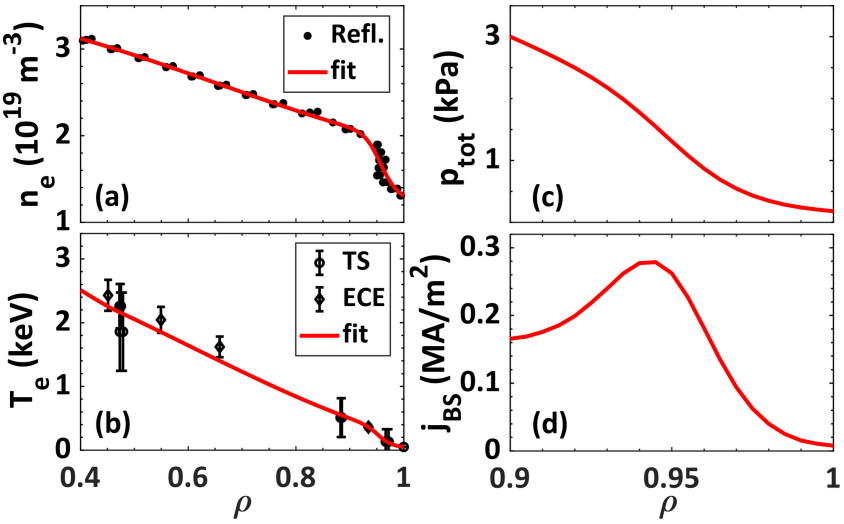

Figure 7. Pedestal profiles, including (a) electron density ne, (b) electron temperature Te, (c) total pressure p_{tot} and (d) bootstrap current density j_{BS}.

The electron density profile n_e shown in Figure 7(a) was measured via microwave reflectometry [22], and its line-integrated value was cross-calibrated with POINT diagnostic data [23]. The relatively high ratio of separatrix-to-pedestal electron density ($n_{e,\mathrm{sep}}/n_{e,\mathrm{ped}} \approx 63\%$ in figure 8(a)) provides favorable access to the small-ELM operational regime [24]. Due to the unavailability of Thomson scattering data for #150425, the electron temperature profile T_e was adopted from similar long-pulse H-mode discharges and validated against ECE measurements [25,26]. Core ion temperature T_i was obtained from XCS diagnostics [27], while edge $T_i = T_e$ was assumed due to low edge temperature and high collisionality. A flat Z_{eff} profile was fixed to the line-averaged VisBrem diagnostic value [28].

Combined with quasi-neutrality conditions andZ_{eff} data, main-ion and impurity densities were derived, and the total plasma pressure $p_{\mathrm{tot}} = n_e T_e + (n_i + n_{\mathrm{imp}})T_i$ was calculated (Figure 7(c)). Given the fully non-inductive nature of the discharge, Ohmic current was neglected, and the pedestal current was dominated by bootstrap current density j_{BS} calculated via the Sauter model [29].

Based on the reconstructed kinetic equilibrium, the VARYPED code was applied to generate equilibrium models by independently scanning pedestal pressure gradients and edge current densities, while keeping stored energy, total plasma current, and plasma shape fixed [30]. The ELITE code was then used to calculate peeling-ballooning mode (PBM) growth rates across a full spectrum of toroidal mode numbers. In the pedestal stability diagram (Figure 8(b)), the horizontal axis represents the peak normalized pedestal pressure gradient α, and the vertical axis denotes half of the normalized maximum edge current density. The stability boundary is defined as the condition where the maximum unstable growth rate divided by half the ion diamagnetic frequency equals unity. The discharge operating point locates in the PBM-stable region near the ballooning boundary, confirming that the long-pulse discharge operates in a stable Type-II small-ELM H-mode regime.

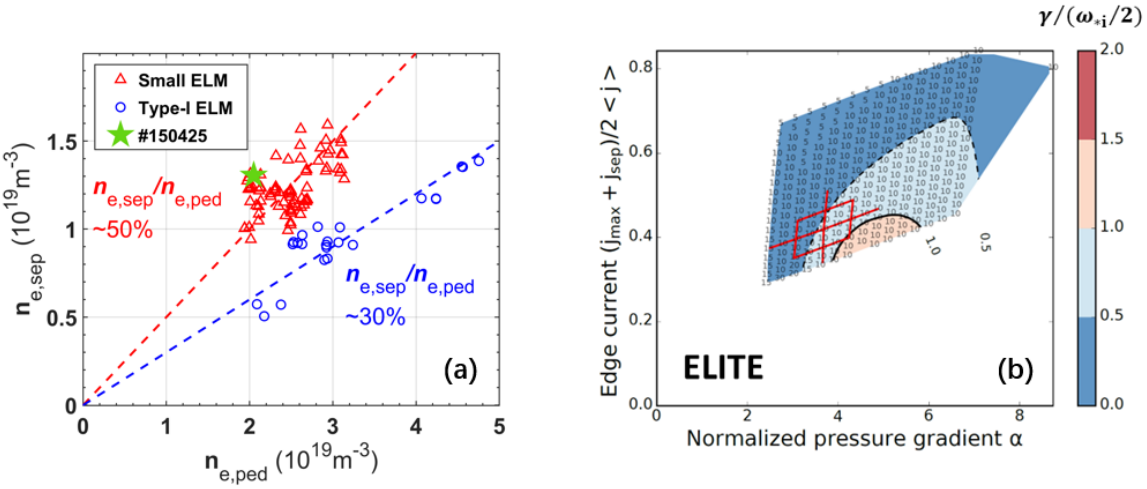

Figure 8. (a)ne_{sep} vs. ne_{ped} in #150425 and other discharges with small and large ELMs. (b) Pedestal stability diagram at about 500s in #150425.

4. Summary and Future Plan

EAST achieved a world-record 1066 s steady-state high-confinement H-mode plasma with 3.05 GJ cumulative injected heating energy, demonstrating kilosecond-scale fully non-inductive operation under reactor-relevant conditions: a full-tungsten all-metal first wall, negligible external momentum input, and electron-dominated RF heating. The key global plasma parameters are summarized as follows: $\beta_P = 2.0$, $f_{\mathrm{BS}} \approx 50\%$, $H_{98,y2} = 1.3$, $n_e/n_G = 0.63$, and spontaneous e-ITB formation without external torque injection. A complete set of integrated engineering solutions was established for long-pulse steady-state operation: actively cooled full-tungsten PFCs for high-power heat exhaust; high-precision long-term magnetic equilibrium and zero loop-voltage control; real-time lithium powder feedback wall conditioning and SMBI multi-channel particle fueling; and optimized small-ELM strike-point positioning for tungsten sputtering mitigation. The core physical mechanisms are fully clarified: LHCD–

ECRH synergistic current drive improves high-density non-inductive current-drive efficiency; the saturated$m/n = 1/1$ kink mode forms a self-organized feedback loop to suppress core turbulence and sustain e-ITB; low plasma rotation eliminates neoclassical tungsten pinch effects, and on-axis ECRH further pumps out tungsten impurities to avoid core high-Z accumulation; wide stable pedestal structures suppress edge PBM instabilities and reduce transient divertor heat loads.

Future EAST upgrades aim to narrow the steady-state performance gap with next-generation fusion reactors, targeting three core objectives for ITER-relevant steady-state scenarios: expanding the plasma operational parameter window, increasing total injected heating power, and optimizing divertor power handling capability. The detailed upgrade plans are listed below.

Plasma geometry and magnetic system upgrades: (1) Enlarging the low-field-side plasma volume and extending the maximum plasma current to 1.0 MA; (2) Adjusting the minor radius to 0.4–0.55 m and optimizing the aspect ratio R/a from 4.3 to 3.6; (3) Increasing PF and IC coil current limits to support higher β_P and long-term equilibrium stability.

RF heating and current-drive system upgrades: (1) Upgrading the 4.6 GHz/4 MW LHW PAM antenna to improve long-distance wave coupling in high-density plasmas; (2) Equipping a dual-frequency ECRH gyrotron system to realize flexible radial current profile$j(r)$ control; (3) Adopting three-strap ICRF antennas to reduce surface electric fields and mitigate impurity sputtering; (4) Raising the total available injected heating power from 12 MW to 18 MW.

Full-tungsten PFC upgrades: (1) Installing a new upper divertor with a BEST-style high-closure cooling structure, achieving a steady-state heat exhaust capacity of 12 MW/m²; (2) Replacing all inner and outer molybdenum wall components with tungsten structures; (3) Upgrading all ICRF and LHW antenna limiters to tungsten monoblock structures.

Upon completion of all hardware upgrades, EAST will target high-performance steady-state H-mode plasmas under total RF heating power of 12–18 MW. The upgraded device will generate a comprehensive experimental database to support the steady-state operation design of ITER and the physical framework construction of CFEDR, laying a solid foundation for future commercial fusion energy development.

References

[1] X. Litaudon et al., Long plasma duration operation analyses with an international multi-machine (tokamaks and stellarators) database, Nucl. Fusion 64, 015001 (2024).

[2] C. Gormezano et al., Chapter 6: Steady state operation, Nucl. Fusion 47, S285-S336 (2007).

[3] Y. X. Wan et al., Overview of the present progress and activities on the CFETR, Nucl. Fusion 57, 102009 (2017).

[4] J. Huang et al., Progress of physics understanding for long pulse high-performance plasmas on EAST towards the steady-state operation of ITER and CFETR, Plasma Phys. Control. Fusion 62, 014019 (2020).

[5] J. Huang et al., Long-pulse high-performance H-mode plasmas achieved on EAST, Phys. Plasmas 30, 062504 (2023).

[6] D. H. Zhu et al., Development of the new lower tungsten divertor for EAST, Nucl. Fusion 60, 016036 (2020).

[7] Q. P. Yuan et al., Plasma control system on EAST, IEEE Trans. Plasma Sci. 46, 1356-1360 (2018).

[8] J. S. Hu et al., Fueling and wall conditioning systems on EAST, Fusion Eng. Des. 84, 2167-2173 (2009).

[9] X. L. Yuan et al., Pellet injection system development for EAST, Fusion Eng. Des. 134, 62-67 (2018).

[10] B. J. Ding et al., Investigations of LHW-plasma coupling and current drive at high density related to H-mode experiments in EAST, Nucl. Fusion 55, 093030 (2015).

[11] Stix T. H., The Theory of Plasma Waves (New York: McGraw-Hill) (1962).

[12] Fisch N. J., Theory of current drive in plasmas, Rev. Mod. Phys. 59, 175 (1987).

[13] Li M. H. et al., Nucl. Fusion 65, 076017 (2025).

[14] W. Wang, L. Q. Xu, X. Z. Gong, et al., Experiment study of m/n = 1/1 mode saturation level in high beta_p discharge on the EAST tokamak, Phys. Plasmas 31, 042103 (2024).

[15] W. Wang, Y. Zhou, L. Q. Xu, et al., Nonlinear MHD simulation of sawtooth crash and saturated steady state regimes in EAST electron heating dominant high beta_p discharge, Eur. Phys. J. D (2026).

[16] L. Xu, S. Lin, C. Mai, et al., Observation of fast electron redistribution during saturated kink mode in high beta_p H-mode discharge with central heating in EAST tokamak, Nucl. Fusion 64, 046024 (2024).

[17] E. Li et al., Experimental evidence of intrinsic current generation by turbulence in stationary tokamak plasmas, Phys. Rev. Lett. 128, 085003 (2022).

[18] I. Krebs, S. C. Jardin, S. Gunter, et al., Magnetic flux pumping in 3D nonlinear magnetohydrodynamic simulations, Phys. Plasmas 24, 102511 (2017).

[19] P. B. Snyder et al., Edge localized modes and the pedestal: A model based on coupled peeling-ballooning modes, Phys. Plasmas 9, 2037 (2002).

[20] T. H. Osborne et al., J. Phys.: Conf. Ser. 123, 012014 (2008).

[21] R. J. Groebner et al., Progress in quantifying the edge physics of the H mode regime in DIII-D, Nucl. Fusion 41, 1789 (2001).

[22] H. Qu et al., Plasma Sci. Technol. 17, 985-990 (2015).

[23] H. Q. Liu et al., Rev. Sci. Instrum. 87, 11D903 (2016).

[24] X. Lin et al., Phys. Rev. A 431, 127988 (2022).

[25] Q. Zang et al., Plasma Sci. Technol. 12, 144-148 (2010).

[26] X. Han et al., Rev. Sci. Instrum. 85, 073506 (2014).

[27] F. D. Wang et al., Rev. Sci. Instrum. 87, 11E342 (2016).

[28] Y. J. Chen et al., Rev. Sci. Instrum. 86, 023509 (2015).

[29] O. Sauter et al., Phys. Plasmas 6, 2834 (1999).

[30] P. B. Snyder et al., Nucl. Fusion 49, 085035 (2009).